


# Speciation and Electronic Structure of $\text{La}_{1-x}\text{Sr}_x\text{CoO}_{3-\delta}$ During Oxygen Electrolysis

Kelsey A. Stoerzinger<sup>1,6,8</sup>  · Xiao Renshaw Wang<sup>2,7</sup> · Jonathan Hwang<sup>1</sup> · Reshma R. Rao<sup>3</sup> · Wesley T. Hong<sup>1</sup> · C. M. Rouleau<sup>4</sup> · Dongwook Lee<sup>1</sup> · Yi Yu<sup>5</sup> · Ethan J. Crumlin<sup>5</sup>  · Yang Shao-Horn<sup>1,2,3</sup> 

## Abstract

Cobalt-containing perovskite oxides are promising electrocatalysts for the oxygen evolution reaction (OER) in alkaline electrolyzers. However, a lack of fundamental understanding of oxide surfaces impedes rational catalyst design for improved activity and stability. We couple electrochemical studies of epitaxial  $\text{La}_{1-x}\text{Sr}_x\text{CoO}_{3-\delta}$  films with in situ and operando ambi-ent pressure X-ray photoelectron spectroscopy to investigate the surface stoichiometry, adsorbates, and electronic structure. In situ investigations spanning electrode compositions in a humid environment indicate that hydroxyl and carbonate affinity increase with Sr content, leading to an increase in binding energy of metal core levels and the valence band edge from the formation of a surface dipole. The maximum in hydroxylation at 40% Sr is commensurate with the highest OER activity, where activity scales with greater hole carrier concentration and mobility. Operando measurements of the 20% Sr-doped oxide in alkaline electrolyte indicate that the surface stoichiometry remains constant during OER, supporting the idea that the oxide electrocatalyst is stable and behaves as a metal, with the voltage drop confined to the electrolyte. Furthermore, hydroxyl and carbonate species are present on the electrode surface even under oxidizing conditions, and may impact the availability of active sites or the binding strength of adsorbed intermediates via adsorbate–adsorbate interactions. For covalent oxides with facile charge transfer kinetics, the accumulation of hydroxyl species with oxidative potentials suggests the rate of reaction could be limited by proton transfer kinetics. This operando insight will help guide modeling of self-consistent oxide electrocatalysts, and highlights the potential importance of carbonates in oxygen electrocatalysis.

---

Kelsey A. Stoerzinger and Xiao Renshaw Wang have contributed equally.

---

✉ Kelsey A. Stoerzinger  
kelsey.stoerzinger@oregonstate.edu

<sup>1</sup> Department of Materials Science and Engineering, Massachusetts Institute of Technology, 77 Massachusetts Avenue, Cambridge, MA 02139, USA

<sup>2</sup> Research Lab for Electronics, Massachusetts Institute of Technology, 77 Massachusetts Avenue, Cambridge, MA 02139, USA

<sup>3</sup> Department of Mechanical Engineering, Massachusetts Institute of Technology, 77 Massachusetts Avenue, Cambridge, MA 02139, USA

<sup>4</sup> Center for Nanophase Materials Sciences, Oak Ridge National Laboratory, Oak Ridge, TN 37831, USA

<sup>5</sup> Advanced Light Source, Lawrence Berkeley National Laboratory, 1 Cyclotron Road, MS6R2100, Berkeley, CA 94720, USA

<sup>6</sup> Physical and Computational Sciences Directorate, Pacific Northwest National Laboratory, 902 Battelle Boulevard, Richland, WA 99354, USA

<sup>7</sup> Present Address: School of Physical and Mathematical Sciences & School of Electrical and Electronic Engineering, Nanyang Technological University, Singapore 637371, Singapore

<sup>8</sup> Present Address: School of Chemical, Biological and Environmental Engineering, Oregon State University, 116 Johnson Hall, Corvallis, OR 97331, USA

## 1 Introduction

Perovskite oxides are promising catalysts for the oxygen reduction and evolution reactions in alkaline media [1–7]. The  $ABO_3$  perovskite crystal structure, where  $A$  is typically a lanthanide or alkaline earth element, and  $B$  a transition metal, can incorporate a wide range of the periodic table and resultant electronic properties [8]. This flexibility makes the structure of particular interest in the study of oxide electrocatalysts, where the search for electronic descriptors for activity aims to guide the rational design of more active catalysts [9–12].

In particular, cobalt-containing perovskite oxides can be highly active catalysts for the oxygen evolution reaction (OER) [4, 6, 13–17]. Substitution of  $Sr^{2+}$  at the  $A$ -site for  $La^{3+}$  leads to nominal oxidation of Co and incorporation of oxygen vacancies [18, 19], with drastic impacts on the material's conductivity [20–23], redox potential [24], and catalytic activity [22, 25–27]. Recently, studies on  $La_{1-x}Sr_xMnO_3$  single crystal thin films [28] and  $La_{1-x}Sr_xCoO_{3-\delta}$  powders [22] have shown that higher conductivity [17] promotes oxygen electrocatalysis activity. However, conductivity is a product of two variables, namely carrier density (the amount of free charges in a unit volume) and carrier mobility (how free and mobile the charges are), and the role of these two variables have yet to be disentangled in oxygen electrocatalysis. Furthermore, changes in the electronic structure lead to different proposed reaction mechanisms for the OER [29]. Sr incorporation increases covalency through the overlap of Co  $3d$  and O  $2p$  states, leading to pH-dependent OER activity as the rate limiting step switches to one proposed to involve  $OH^-$  adsorption onto oxygen sites [30]. Missing, however, is direct observation of reaction intermediates under conditions relevant to electrocatalysis and the resultant changes in electronic structure.

Ambient pressure X-ray photoelectron spectroscopy (AP-XPS) allows the study of oxide surfaces in a humid environment in situ [31–34]. The ability to change the relative humidity (RH) via the water partial pressure and sample temperature allows for rigorous deconvolution of the surface adsorbates which form from reaction with water [35]. An AP-XPS comparison of  $LaBO_3$  perovskite catalysts elucidated that the coverage of hydroxyl species (OH) at a fixed RH scaled with the binding strength calculated with density functional theory (DFT), and the affinity for OH trended inversely with activity for the oxygen reduction reaction (ORR) [36]. Recent advances in AP-XPS using “tender” X-rays has enabled the study of electrocatalysts in operando, employing a dip-and-pull method to generate an electrolyte meniscus through which photoelectrons can pass [37]. This approach can

characterize the electrocatalyst surface in parallel with the electrolyte [38, 39], shedding light on surface speciation and details of the electrochemical potential's distribution in the electrocatalyst (band bending [40]) and electrolyte (double layer [41]).

Here, we study epitaxial films of (001)-oriented  $La_{1-x}Sr_xCoO_{3-\delta}$  surfaces ( $x=0, 0.2, 0.4, 0.5, 0.6$ ) as electrocatalysts for the OER in alkaline electrolyte. The thin film geometry enables the parallel study of intrinsic activity, carrier density and mobility, and surface speciation to develop a comprehensive understanding of the relationship between electronic structure and reactivity. We couple two AP-XPS approaches: in situ in a humid environment (ALS 9.3.2), and operando (ALS 9.3.1) at OER conditions in KOH electrolyte. The tailored information depths ( $\sim$  few and  $\sim 10$  s of nm, respectively) of each approach gives additional confidence to our assignment of surface adsorbates under operating conditions, while also probing the voltage drop across the solid/liquid interface. Comparing films of different Sr contents in a humid environment, the affinity for  $OH^-$  increases with Sr, reaching a maximum at  $La_{0.6}Sr_{0.4}CoO_{3-\delta}$  (referred to here as Sr40). Sr40 is associated with the greatest carrier concentration and mobility and also exhibits the highest OER activity of the film compositions tested. Operando consideration of an electrocatalyst with 20% Sr doping ( $La_{0.8}Sr_{0.2}CoO_{3-\delta}$ , referred to here as Sr20) indicates that hydroxyl species persist under both ORR and OER conditions, as do carbonate ( $CO_3$ ) adsorbates, for which perovskite oxides have a high affinity. The surface remains stable with no appreciable change in stoichiometry at any applied potential, and behaves as a metal with the voltage drop occurring in the electrochemical double layer. This new insight into the operating surface chemistry of a perovskite during oxygen electrocatalysis supports previously proposed mechanisms involving hydroxylated surfaces, and suggests the affinity for carbonate may impact the number of available sites or binding strength through possible adsorbate–adsorbate interactions. The relation between both high carrier concentration (related to band structure) and high carrier mobility (related to metal–oxygen covalency) with greater OER activity and more hydroxylation illustrates the importance of hole carrier availability in both processes.

## 2 Experimental

### 2.1 Thin Film Fabrication and Characterization

High quality  $La_{1-x}Sr_xCoO_{3-\delta}$  (LSCO) thin films were fabricated by pulsed laser deposition (PLD) on (001)  $SrTiO_3$  (STO) substrates having a  $La_{0.7}Sr_{0.3}MnO_3$  (LSMO) buffer layer (substrates for the 9.3.2 measurements were supplied by Crystec while those and for the 9.3.1 measurements were

supplied by Princeton Scientific). Films were grown additionally for all Sr concentrations without the LSMO buffer layer for Hall measurements, and for Sr20, it was grown in a range of  $p(\text{O}_2)$  on STO as well as on other substrates [ $\text{LaAlO}_3$  (LAO) and  $(\text{LaAlO}_3)_{0.3}(\text{Sr}_2\text{AlTaO}_6)_{0.7}$  (LSAT); Princeton Scientific Inc.] to consider the impact of the electronic properties on OER activity. The as-received substrates exhibit a smooth surface with atomic terraces visible under atomic force microscopy (AFM). PLD was performed using a KrF excimer laser ( $\lambda = 248$  nm) with a laser fluence at the target surface of  $\sim 1\text{--}1.98$  J/cm<sup>2</sup>. Sintered LSCO and LSMO polycrystalline targets were used for ablation. The films were fabricated at 500–550 °C (635 °C for the 9.3.1 measurements) in  $p(\text{O}_2)$  of 50 mTorr. The 15 nm film and 15 nm buffer layer thickness (45 nm and 45 nm, respectively, for the 9.3.1 measurements) were carefully controlled by number of laser shots, and subsequently the samples were cooled to room temperature under the growth  $p(\text{O}_2)$ .

The crystal structure of the films and LSMO buffer layer were examined using X-ray diffraction (XRD) (Bruker), and showed the LSCO films and LSCO films grown on LSMO buffered STO were epitaxial (Fig. S1) for all growth conditions explored here. Film surface morphologies were examined by AFM in tapping mode (Nanoscope IV, Veeco Metrology), and the root mean square (RMS) roughness was measured to be  $\sim 0.2$  nm. Conductivity was measured with samples contacted in a Van der Pauw geometry [42], and carrier mobility and concentration were measured at room temperature by Hall effect (magnetic field swept from  $-1$  to  $+1$  T).

For electrochemical measurements, including operando measurements on 9.3.1, the electrode was electrically contacted by scratching gallium–indium eutectic (Sigma-Aldrich, 99.99%) into a small corner of the film to reach the LSMO layer, and a Ti wire (Sigma-Aldrich, 99.99%) was affixed with silver paint (Ted Pella, Leitsilber 200). The back and sides of the electrode, as well as the wire, were covered with a non-conductive, chemically resistant epoxy (Omegabond 101), so only the catalyst surface was exposed to the electrolyte [17].

## 2.2 Ex Situ Electrochemical Measurements

Electrochemical measurements to determine the intrinsic OER activity were performed with a Biologic SP-300 potentiostat in a  $\sim 125$  mL solution of 0.1 M KOH, prepared from deionized water (Millipore,  $> 18.2$  M $\Omega$  cm) and KOH pellets (Sigma-Aldrich, 99.99%). Potentials were referenced to either a saturated Ag/AgCl or saturated calomel electrode (Pine), both calibrated to the reversible hydrogen electrode (RHE) scale in 0.1 M KOH. Potentials were corrected for the electrolyte/cell resistance from the high frequency intercept of the real impedance ( $\sim 45$   $\Omega$ ).

Measurements of the OER (referred to as “ex situ” given that no spectroscopy was performed in parallel with these measurements) were conducted in 0.1 M KOH electrolyte presaturated by bubbling O<sub>2</sub> for  $\sim 30$  min and under continuous O<sub>2</sub> bubbling (Airgas, ultrahigh-grade purity) to fix the equilibrium potential. Cyclic voltammetry (CV) scans were carried out at a sweep rate of 10 mV/s, starting and finishing at open circuit voltage, sweeping from 1.2 up to 1.65 V versus RHE for the OER.

## 2.3 Ambient Pressure XPS in Gas Phase H<sub>2</sub>O

In situ AP-XPS was collected at Beamline 9.3.2 [43] at Lawrence Berkeley National Laboratory’s (LBNL) Advanced Light Source (ALS). Films were placed onto a ceramic heater, with a thermocouple pressed into Au foil mounted directly onto the sample surface for temperature measurements, and isolated from the sample holder clips with an Al<sub>2</sub>O<sub>3</sub> spacer. The energy scale was calibrated at each incident photon energy via the Au 4f (84 eV) peak. To ensure the trends presented here were not artifacts of ionizing radiation, we checked that the O 1s spectra was the same between an irradiated spot and that of fresh spots that had not been exposed to the X-ray beam prior to a quick acquisition (Fig. S2).

For in situ measurements (9.3.2), the samples were cleaned by heating to 300 °C in a  $p(\text{O}_2)$  of 0.1–0.3 Torr (measured by a calibrated capacitance gauge) until the carbon level remained unchanged, as indicated by the C 1s spectra. After characterization of the clean surface in 0.1 Torr O<sub>2</sub>, the chamber was evacuated to a pressure  $< 2 \times 10^{-7}$  Torr, and a  $p(\text{H}_2\text{O})$  of 0.1 Torr was introduced into the chamber. The H<sub>2</sub>O was prepared from deionized water (Millipore,  $> 18.2$  M $\Omega$  cm) and degassed by several freeze–pump–thaw cycles. The sample was then cooled in increments of 25 °C down to a final temperature of 25 °C, keeping the chamber pressure constant at a  $p(\text{H}_2\text{O})$  of 0.1 Torr. At every temperature, the O 1s and C 1s core level spectra were collected at 735 and 490 eV incident photon energy, respectively, and at 100 °C increments as well as 25 °C, the La 4d, Sr 3d, and Co 3p core level spectra were also collected at 735 eV. Additional spectra were collected at a lower incident photon energy of 690 or 350 eV (for oxygen and metal core levels, respectively) to tune the cross section and information depth at 300 °C in O<sub>2</sub> and H<sub>2</sub>O, as well as at 25 °C in H<sub>2</sub>O following the isobar.

## 2.4 Ambient Pressure XPS in Alkaline Electrolyte

Operando AP-XPS was collected at Beamline 9.3.1 [37] at the ALS. The photon energy was fixed to 4.0 keV (calibrated via the Au 4f peak) and collected at normal emission. The electrolyte was prepared from deionized water

(18.2 M $\Omega$  cm) and KOH (99.99%, Aldrich). Before its introduction into the experimental chamber, the 0.1 M electrolyte was outgassed for at least 30 min at low pressure ( $\sim 10$  Torr) in a dedicated off-line chamber. Once the manipulator with the mounted sample and Pt foil counter electrode, as well as the outgassed electrolyte, were placed into the experimental chamber, the pressure was lowered carefully to the water vapor pressure (16–17 Torr at room temperature).

Electrochemical measurements were conducted with a Biologic SP-300 potentiostat. The sample was first fully immersed and cycled three times at 20 mV/s from  $-0.25$  to  $0.9$  V versus the Pt counter electrode ( $\sim 0.75$ – $1.9$  V vs. the RHE). Subsequently, the dip-and-pull procedure was carried out to obtain a stable and conductive nanometers-thick electrolyte layer on the Sr20 surface, and the electrode was cycled two times. The electrode was then polarized at the noted potentials, and AP-XPS collected while the current was at steady state. In order to maintain a similar meniscus thickness and compensate for evaporation over time from active pumping, the height of the electrolyte reservoir was adjusted periodically.

### 3 Results and Discussion

#### 3.1 Sr-Dependent OER Activity

Though multiple studies have considered the OER activity of LSCO in powdered form [22, 26], the presence of grain boundaries, uncertainty in surface area, and heterogeneous crystallographic termination can convolute measurement of both electronic properties and OER performance. We have prepared epitaxial thin films of  $\text{LaCoO}_{3-\delta}$  (Sr0),  $\text{La}_{0.8}\text{Sr}_{0.2}\text{CoO}_{3-\delta}$  (Sr20),  $\text{La}_{0.6}\text{Sr}_{0.4}\text{CoO}_{3-\delta}$  (Sr40),  $\text{La}_{0.5}\text{Sr}_{0.5}\text{CoO}_{3-\delta}$  (Sr50), and  $\text{La}_{0.4}\text{Sr}_{0.6}\text{CoO}_{3-\delta}$  (Sr60), among which the study of epitaxial Sr0 has previously shown good agreement with rotating disk electrode measurements on Sr0 powder [17]. A representative reciprocal space map shown for Sr50 in Fig. 1a illustrates the epitaxial nature of the LSCO film and LSMO buffer layer with the  $\text{SrTiO}_3$  substrate, both of which remain coherently strained to the cubic substrate. A representative AFM shown in Fig. 1b illustrates the smooth surface with visible atomic terraces.

The OER activity measured in a three-electrode cell increases upon substitution of  $\text{Sr}^{2+}$  for  $\text{La}^{3+}$  in LSCO up to Sr40, subsequently decreasing with further Sr incorporation. Figure 2a shows the second cycle of CV for LSCO thin films on  $\text{SrTiO}_3$  substrates as a function of Sr concentration in 0.1 M KOH (for Tafel analysis, see Table S1), where the activity can be quantified as the capacitance corrected current density at a given applied potential, shown in Fig. 2b to be maximum for Sr40. In addition, Fig. 2b shows the conductivity of LSCO films also exhibits a maximum at

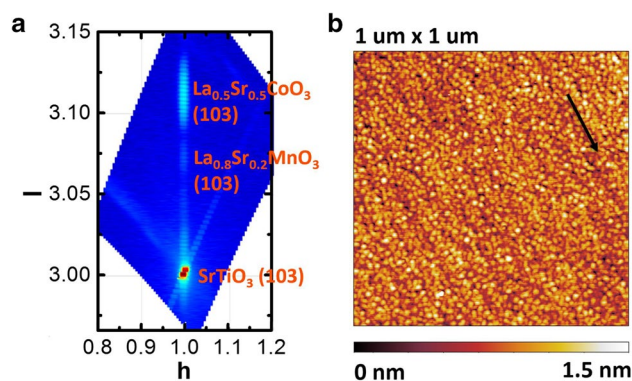


**Fig. 1** **a** Reciprocal space mapping on representative  $\text{La}_{0.5}\text{Sr}_{0.5}\text{CoO}_{3-\delta}$  (Sr50) grown on  $\text{La}_{0.8}\text{Sr}_{0.2}\text{MnO}_3$  buffered  $\text{SrTiO}_3$  substrates. All films are structurally homogeneous with in-plane lattice parameters matching that of  $\text{SrTiO}_3$ . **b** AFM image of sample morphology. Surface roughness is  $\sim 0.2$  nm, with visible atomic terraces, the direction along which is indicated by the arrow

Sr40. Moreover, in order to maximize the span of carrier density and carrier mobility, we have also grown LSCO on substrates with different in-plane lattice parameters ( $a_{\text{LAO}} = 0.382$  nm,  $a_{\text{LSAT}} = 0.387$  nm, and  $a_{\text{STO}} = 0.39$  nm) and at different  $p(\text{O}_2)$  (0.5, 5, 50 and 500 mTorr), the activity of which is presented in Fig. S3. Interestingly, high OER activity is found for films which have both high carrier density and high mobility (Fig. 2c). We further evaluated the relative influence of the carrier density and carrier mobility on the OER activity using ordinary least-squares regression (Table S2). The regression results indicate that both carrier density and carrier mobility have a non-negligible impact on the OER activity and are equally important for the OER activity. Similar trends with a maximum activity at intermediate Sr contents have been observed for LSCO powders, attributed to the overlap of unoccupied Co 3d conduction bands and occupied O 2p valence bands (VBs) that lead to improved conductivity in pressed pellets [26]. Others have observed that the activity continually increases with Sr content in LSCO particles, where metal–oxygen covalency was correlated with an increase in oxygen ion diffusivity [22] and a predicted change in reaction mechanism. In contrast, others have proposed that not only the band curvature (where curvature reflects the delocalization of charge and cation–anion covalency [44]) [45] but also the band structure, such as oxygen 2p-band filling [10, 16] impacts oxygen electrocatalysis, however the extent of influence has been challenging to disentangle. Recent findings have demonstrated that compared to  $\text{LaCoO}_3$ , the covalent nature (band overlap) of Co 3d and O 2p bands in  $\text{SrCoO}_3$  and the accessibility of the O 2p band to redox (band filling) lead to a different OER mechanism involving lattice oxygen and an increase in OER activity [30]. This change in band structure with Sr-incorporation in LSCO also leads to an increase in conductivity, as increasing



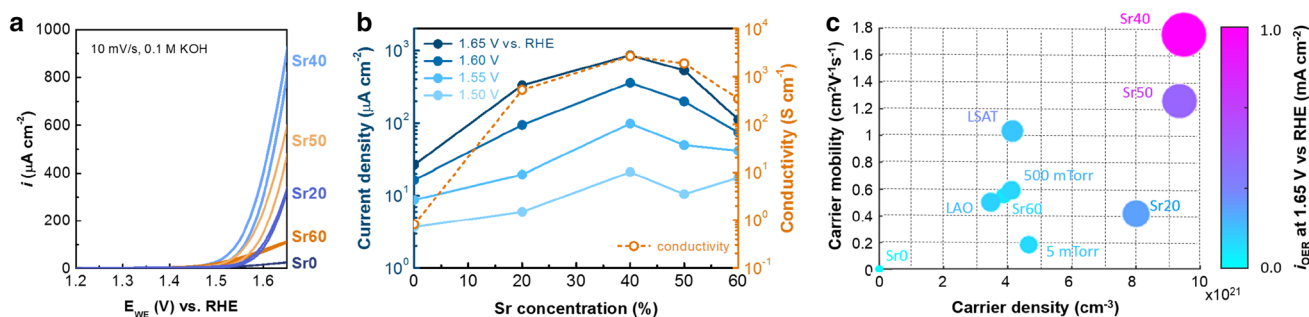


**Fig. 2** **a** Second cycles of CV of LSCO thin films on SrTiO<sub>3</sub> substrates as a function of Sr concentration in pH=13. The scan rate is 10 mV/s and potentials are reported on the RHE scale. **b** Left axis (solid): OER current density at the noted potential on the RHE scale as a function of Sr concentration (SrTiO<sub>3</sub> substrates). Right axis (open): electrical conductivity of LSCO as a function of Sr concen-

tration. **c** Current density at 1.65 V versus RHE in a map of carrier density (holes) and carrier mobility. The area of the dots in the activity map is proportional to the OER current density at 1.65 V versus RHE. The substrate is SrTiO<sub>3</sub>, unless otherwise noted for Sr20 grown on LAO or LSAT. The  $p(\text{O}_2)$  during growth was 50 mTorr unless otherwise noted for Sr20 deposited at 5 or 500 mTorr

metal–oxygen covalency decreases the localization of charge-carrying holes and their effective mass (increasing carrier mobility) [46]. We emphasize that a comprehensive view of band structure is most informative in understanding OER activity; for instance a perspective considering only conductivity would predict the half metal La<sub>0.8</sub>Sr<sub>0.2</sub>MnO<sub>3</sub> active for OER, when it is in fact relatively inactive [47].

### 3.2 Sr-Dependent Surface Reactivity of (001)-Oriented Sr-Substituted LaCoO<sub>3- $\delta$</sub> with H<sub>2</sub>O Vapor

We next consider the surface speciation of the LSCO catalysts to better understand the link between electronic structure and catalytic activity. In situ studies in a humid environment enable the surface species to be identified by changing the chemical potential of water, which will in turn aid in understanding the active surface in operando. The O 1s spectra of perovskite oxide surfaces in Fig. 3, S4, and S5 are a convolution of numerous species [48, 49]. In a humid or aqueous environment, these include the oxide lattice, hydroxyl species, undercoordinated oxygen, adsorbed water, and oxygen-containing carbonaceous species (such as carbonates), which overlap in binding energy (BE) [31, 50]. Furthermore, it can be challenging to separate these contributions from that of liquid water in the aqueous phase. Some of these species, such as hydroxyls, can also be affiliated with distinct features in the metal spectra [51]. In order to disentangle these species, we consider the oxygen and metal core levels as a function of the chemical potential of water (by changing the RH), and as a function of Sr<sup>2+</sup> substitution for La<sup>3+</sup> (resulting in Co oxidation and the presence of oxygen vacancies). The resultant global fit can then be employed in operando measurements to better understand the surface speciation in an aqueous environment.

Four La<sup>3+</sup>/Sr<sup>2+</sup> composition ratios were considered to understand how the resultant oxidation of Co and/or presence of oxygen vacancies impacts surface speciation. The A-site ratios measured at the surface trend as expected with target stoichiometry, and both A- and B-site ratios remain constant across the range of temperatures and atmospheres studied (Figs. S6, S7, S8). Figure 3 compares the O 1s spectra for Sr0, Sr20, Sr40, and Sr60 in dry conditions (300 °C, 0.1 Torr O<sub>2</sub>) and ~0.3% RH (25 °C, 0.1 Torr H<sub>2</sub>O). The O 1s spectra of the LSCO chemistries in dry conditions (Fig. 3a–d) are similar: the bulk peak is dominant, strongly bound OH species persist to similar extents, and some oxidized carbon persists (where the C 1s inset was used in quantifying an upper bound for the O 1s CO<sub>3</sub> peak). For Sr60, some additional intensity at ~3 eV above bulk BE is attributed to other surface species such as undercoordinated oxygen [52].

The species present on the surface evolve with changes in H<sub>2</sub>O activity, probed in an isobaric measurement (Fig. S4). At low RH, the O 1s spectra is primarily comprised of one main peak with a high BE shoulder. Depth profiling (Fig. S5) indicates the low BE feature is located in the bulk, and is thus attributed to the oxide lattice. Increasing RH leads to an increase in a feature ~1.6 eV higher BE than that of the bulk, attributed to hydroxyl species (OH). At sufficiently high RH, water adsorbs onto the surface (H<sub>2</sub>O<sub>ads</sub>) at ~4.6 eV higher BE. The high affinity of La/Sr-containing perovskite oxides for carbonate [53] results in their formation in humid environments from residual CO<sub>2</sub> in the chamber or water, evident from the rise in C 1s intensity at ~289 eV and commensurate rise in O 1s at ~3 eV above the bulk BE. This feature was fit quantitatively by experimental calibration of the C:O intensity ratio of CO<sub>2</sub> gas, with a relative error determined from the standard deviation in CasaXPS to be ~1%. Some residual intensity remained at ~2.8 eV above the bulk, attributed to a “surface” species, such as undercoordinated

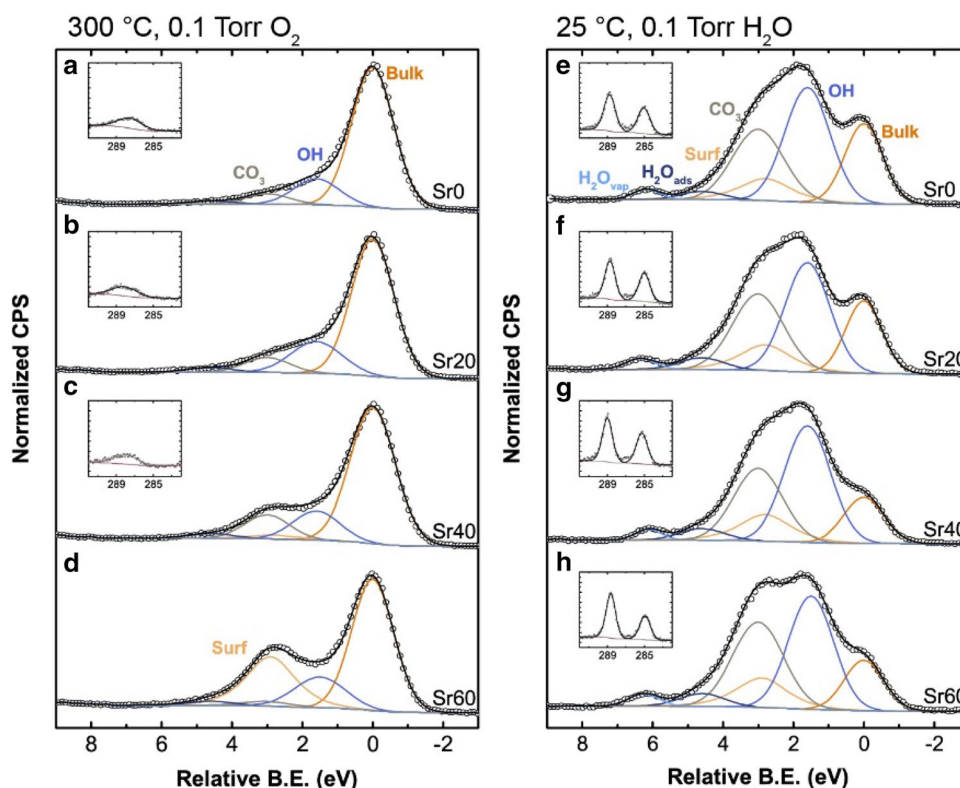


**Fig. 3** O 1s (735 eV incident photon energy) and C 1s (490 eV incident photon energy, inset) spectra for LSCO of noted Sr concentration on a binding energy scale relative to the bulk peak (orange). O 1s spectra are normalized to the maximum intensity, which is the bulk peak at 300 °C in 0.1 Torr O<sub>2</sub> (a–d) and the OH peak at 25 °C in 0.1 Torr H<sub>2</sub>O (e–h). The C 1s spectra are on an absolute, shared scale. The CO<sub>3</sub> peak in the C 1s at ~289 eV is used to fix the intensity of the CO<sub>3</sub> peak in the O 1s spectra at 3 eV offset (gray), a simi-

lar location to the “surface” peak (peach, +2.8 eV), which is fit freely from the remainder. The OH peak (medium blue) grows with RH, and water adsorbs (H<sub>2</sub>O<sub>ads</sub>, dark blue) at high RH. The H<sub>2</sub>O gas phase peak (light blue) is well-separated from the oxide peaks. Unfortunately, the C 1s spectra was not collected for Sr60 in 0.1 Torr O<sub>2</sub> (d), but C 1s spectra before/after this condition indicated similar trends to the other chemistries

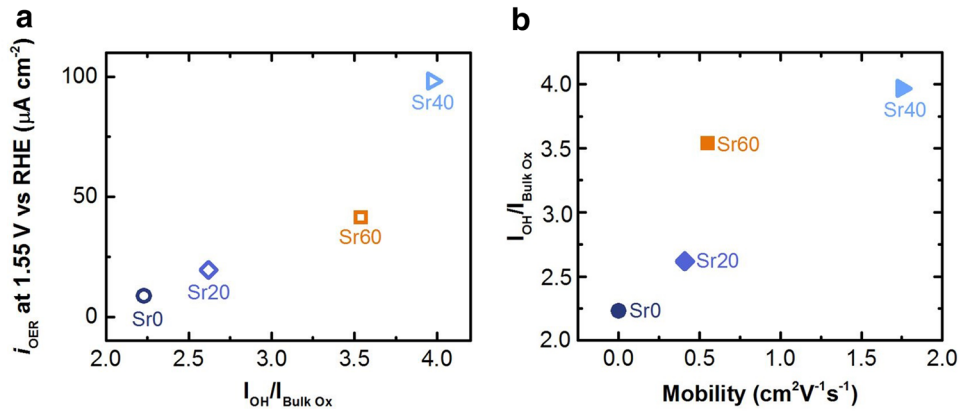
oxygen like (protonated) peroxy groups or hydroxyls on the La/Sr site [52]. The gas phase water peak (H<sub>2</sub>O<sub>vap</sub>) is well isolated from the surface species >6 eV above the bulk BE. The best fit obtained from comprehensively considering the water isobars of the LSCO series is presented in Table S3.

The surface speciation varies notably with Sr content in humid environments (Fig. 3e–h), probed with great surface sensitivity due to the small mean-free path ~4.5 Å of O 1s photoelectrons [35]. The affinity for hydroxyl species can be approximated by the ratio between the OH and bulk peak, which increases with Sr, exhibiting a maximum at Sr40. Similarly, the ratio of the CO<sub>3</sub> (fixed by the C 1s intensity) and “surface” features relative to the bulk also increase with Sr content at high RH. The formation of surface adsorbates may be driven by the surface reducibility, where higher Sr contents lead to more Co<sup>4+</sup> sites that can be reduced under conditions of high RH by e.g. OH adsorption. Another potential driving force could be the filling of surface oxygen vacancies, favored with higher Sr contents, where a larger vacancy concentration could lead to more available sites for

hydroxyl formation. Both are supported by comparing X-ray absorption measurements at the O K-edge and Co L-edge in dry and humid environments (Fig. S9). Two aspects of surface speciation remain similar across Sr content: the amount of adsorbed water (H<sub>2</sub>O<sub>ads</sub>), and the location of the gas phase (H<sub>2</sub>O<sub>vap</sub>) peak relative to the bulk, which suggests a similar surface work function or surface dipole [54]. The comparable location of H<sub>2</sub>O<sub>vap</sub> is in agreement with polar surface species such as OH<sup>-</sup> adsorbing to equilibrate the surface Fermi level with that of the humid environment.

Consideration of the OER activity and electronic properties brings further insight into the observed surface speciation. Hydroxylation—the extent of which is proportional to the ratio of the OH peak to the bulk oxide peak—trends with OER activity at lower overpotentials (Fig. 4a), suggesting that the formation of hydroxyl intermediates does not hinder OER, in contrast to ORR [36]. Furthermore, the extent of hydroxylation trends more so with carrier mobility (Fig. 4b) than with conductivity (Fig. S10), indicating that the ability of holes to react at

**Fig. 4** **a** The OER current at 1.55 V versus RHE measured in 0.1 M KOH increases with hydroxylation, reflected in the intensity of OH/bulk oxide measured at 25 °C in 100 mTorr H<sub>2</sub>O using AP-XPS (735 eV incident photon energy). **b** Hydroxylation measured with AP-XPS increases with LSCO mobility

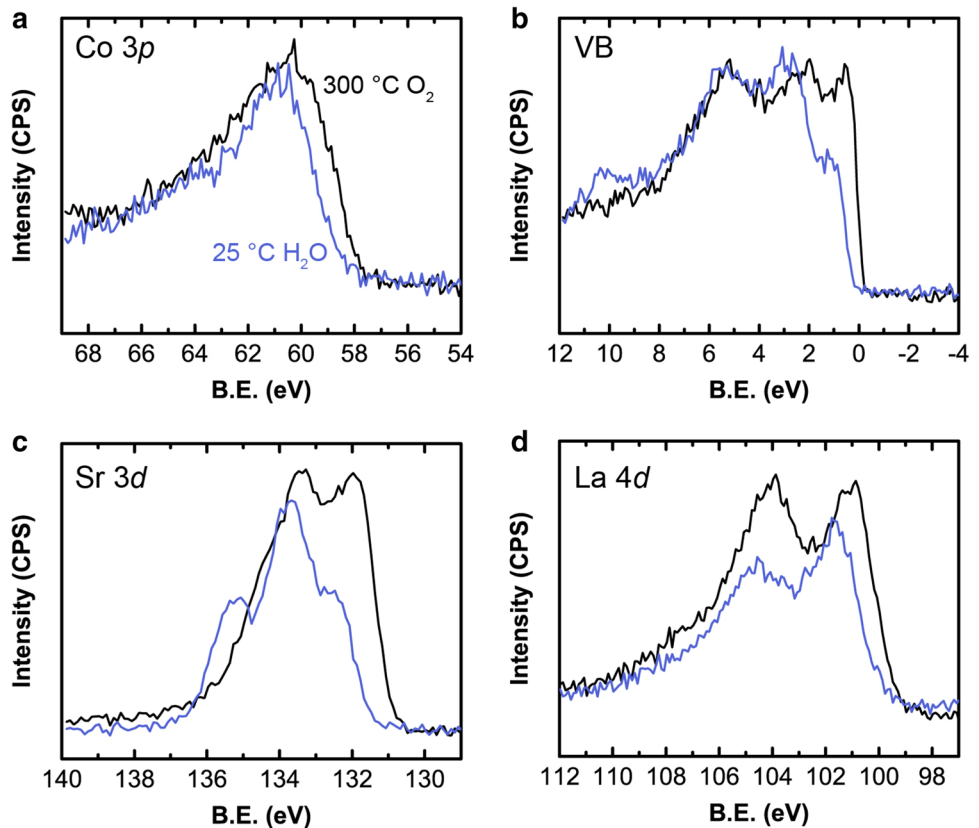


the surface plays an important role in the adsorption of OH<sup>-</sup> species. The relation between carrier mobility and metal–oxygen covalency then suggests that hydroxylation may be promoted by a high degree of overlap between the O 2*p*-band and the Co 3*d*-states. This is consistent with the increase in the point of zero charge from Sr0 to Sr40 [3], indicating a lowering of the Fermi level with Sr incorporation results in the accumulation of negatively charged hydroxyls in order to equilibrate with oxygen redox.

### 3.3 Impact of Speciation on Surface Dipole/Band Bending

Changes in surface speciation can result in the formation of surface dipoles, causing surface band bending, in addition to differences in the electronic structure. We here assess the potential for band bending and/or the formation of a surface dipole by changes in the core level BEs for Sr20, where the BE scale is calibrated to the surface Fermi level. Figure 5 presents the Co 3*p*, Sr 3*d*, La 4*d*, and VB, compared at the two extremes of RH. In comparison to dry conditions (300 °C in 0.1 Torr O<sub>2</sub>),

**Fig. 5** La<sub>0.8</sub>Sr<sub>0.2</sub>CoO<sub>3- $\delta$</sub>  (Sr20) at 300 °C in 0.1 Torr O<sub>2</sub> (black) and at 25 °C in 0.1 Torr H<sub>2</sub>O (blue) probed at 350 eV incident photon energy. Shifts to higher binding energy with RH are observed for the **a** Co 3*p*, **b** valence band, **c** Sr 3*d* (see Fig. S11 for depth profiling) and **d** La 4*d*, consistent with downward band bending or the formation of a surface dipole



at high humidity (25 °C in 0.1 Torr H<sub>2</sub>O) all core levels shift to higher BE. For the Co 3*p*, the increase in BE may be linked to the narrowing of the full width at half maximum (FWHM), suggesting changes in surface speciation impact the Co valence. The increase in BE of the VB edge is tied to a reduction in intensity at ~1 eV, attributed to overlap between the Co 3*d* and O 2*p* states [55, 56]. An additional feature is also observed at high RH ~10 eV, possibly arising from the presence of hydroxyls on the surface [57]. The Sr 3*d* both increases to higher BE and changes the weighting between surface and bulk features, with more “surface” component at higher RH (Fig. S11) [58], suggesting OH species and/or CO<sub>3</sub> species adsorb on Sr sites. Changes in the La 4*d* are more subtle, arising from differences in hybridization between the La and O as the surface becomes more ionic from hydroxylation [59]. These shifts to higher BE, not observed for the C 1*s* (Fig. S12) as the sample is grounded by the thermocouple in contact with the topmost surface, could arise from downward band bending relative to the dry condition, as core levels move farther from the Fermi level. However, the increase in BE shows minimal depth dependence (Fig. S12), indicating that either band bending occurs primarily over the shortest information depth (IMFP~5.6 Å for O 1*s* at 690 eV incident photon energy), or that the shift primarily arises from the intrinsic dipole of the OH<sup>-</sup> adsorbates [60], where we note the shift in BE trends with the hydroxyl content on the surface (Fig. S12). The conductive nature of Sr20 from Hall measurements also suggests the shift in BE originates not from the electrostatic build-up of charge within the film, but rather from the formation of a surface dipole due to the adsorption of hydroxyl species. To investigate this explicitly, we turn to measurements involving a fully formed electrostatic double layer with operando measurements of Sr20.

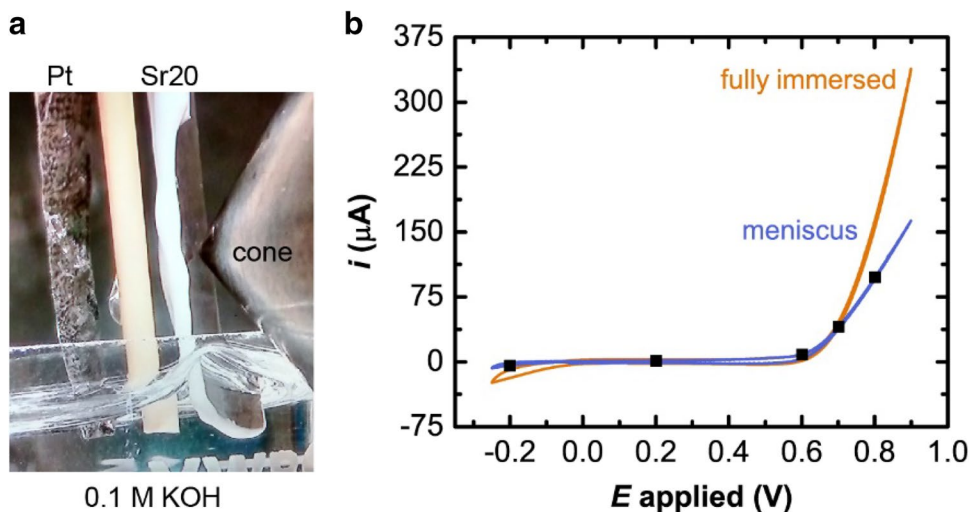
### 3.4 Ambient Pressure XPS in Operando

Aided by an understanding of the surface species present in humid conditions, we next consider the speciation of Sr20 in operando with a 0.1 M KOH electrolyte, as shown in Fig. 6. The sample is polarized relative to a Pt counter electrode, where 0 V applied is ~1 V versus RHE, and exhibits the expected onset of the OER at ~0.65 V applied. At potentials of the ORR around -0.2 V applied, initial ORR current decreases as the electrolyte is not saturated with oxygen gas. For operando AP-XPS measurements, the electrode is partially withdrawn from the electrolyte reservoir, leading to a thin meniscus of electrolyte through which the 4 keV incident photon energy beam passes. We consider the surface under five applied potentials: ORR conditions at -0.2 V, approximately open circuit at 0.2 V, just before the onset of OER at 0.6 V, just after the onset of OER at 0.7 V, and at more oxidizing potentials of 0.8 V versus the Pt counter electrode.

#### 3.4.1 Identifying Surface Species

To fit the O 1*s* spectra of Sr20 in operando, we use the understanding obtained from the water isobar experiments on the LSCO series in situ (Table S3). We modify the fit in two ways: (1) the CO<sub>3</sub> peak is not constrained in intensity from the C 1*s* spectra due to its unknown cross section and thus could also contain some “surface” oxygen species, and (2) the location of the liquid-phase water peak (H<sub>2</sub>O<sub>liq</sub>) was allowed to vary—in contrast to the adsorbed water peak of in situ measurements—as it will change due to the voltage drop which forms across the electrolyte when the sample is polarized. Figure 7 shows the O 1*s* spectra as a function of applied potential, normalized to the bulk oxide peak. Some variation of the water layer occurs over time due to evaporation, compensated for by periodically changing the height of

**Fig. 6** **a** Photograph of the operando setup at ALS beamline 9.3.1 for Sr20. The sample was fully immersed and cycled vs. Pt counter electrode (orange in panel **b**), and then withdrawn to form a stable meniscus of 0.1 M KOH electrolyte (blue in panel **b**), where photoelectrons were collected by the cone. **b** The potentials for analysis are indicated with black squares atop the meniscus CV, performed at 10 mV/s. The applied voltage of 0 V is ~1 V versus RHE





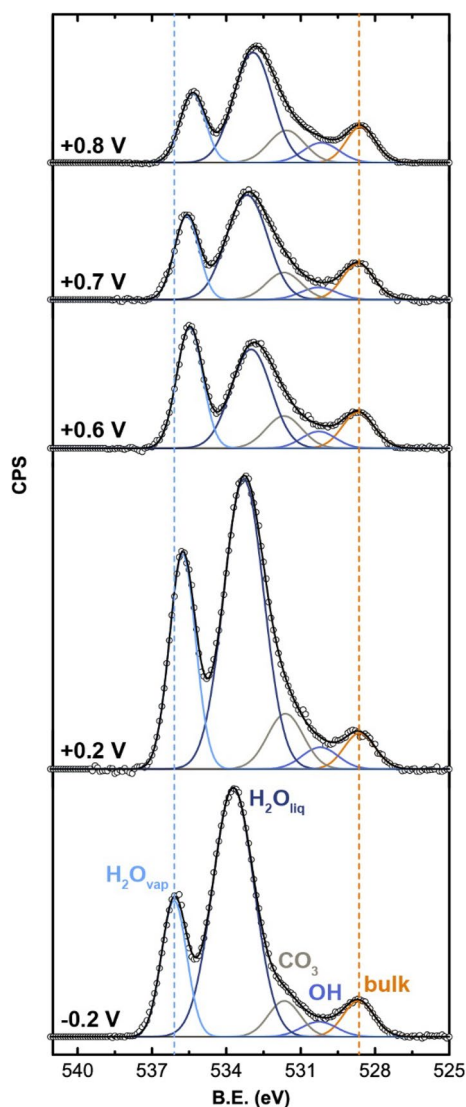


**Fig. 7** Background subtracted O 1s spectra for Sr20 at noted applied potentials. Some change in water layer thickness ( $\text{H}_2\text{O}_{\text{liq}}$ , dark blue) due to evaporation impacts the attenuation of the oxide signal (Fig. S13); therefore spectra are normalized to the intensity of the bulk oxide peak. The bulk peak (orange) is tied energetically to the analyzer and does not shift, in contrast to the  $\text{H}_2\text{O}$  vapor peak (light blue) which shifts with the applied potential, quantified in Fig. 8. The applied voltage shown versus the Pt counter electrode corresponds to  $\sim 1$  V versus RHE at 0 V versus Pt

the electrolyte reservoir, which does not affect the relative ratio of surface species or BE of species (Fig. S13).

### 3.4.2 Assessing Potential Band Bending

Shifts in the BE of O 1s components in Fig. 7 are indicative of the potential experienced at the solid/liquid interface. As the sample is grounded to the analyzer, leading to a fixed BE of the bulk oxide peak (orange dashed line), a change in applied potential is evident by the shift in BE of the gas

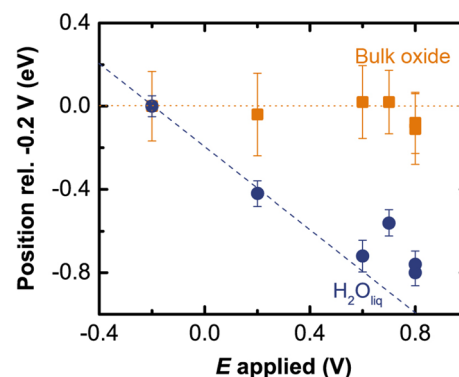


**Fig. 8** Position of the bulk oxide peak (orange squares) and liquid  $\text{H}_2\text{O}$  peak (blue circles) of Sr20 as a function of applied potential, relative to that at  $-0.2$  V. The bulk peak, where the sample is energetically coupled to the analyzer, does not change with bias, however the liquid peak illustrates the difference in sample work function. The dashed line illustrates a 1:1 correspondence between applied potential and BE shift

phase peak ( $\text{H}_2\text{O}_{\text{vap}}$ , blue dashed line), which is not tied to the same vacuum level. At more oxidizing applied potentials, the decrease in gas phase BE is consistent with an increase in the electrode work function (Fig. S14a).

The extent to which the potential difference drops across the electrochemical double layer or within the electrocatalyst can be elucidated through changes in the liquid phase water peak and cation core levels. For Sr20 (Fig. 8), the shift in the liquid phase water peak is initially linear and  $\sim 1:1$  at reducing and low potentials, however it deviates to a lesser shift at oxidizing potentials. This is consistent with the finite width of the electrochemical double layer in the 0.1 M KOH electrolyte, which then contributes to the observed shift in liquid phase [41]. Negligible voltage loss is expected at the Pt counter in the current range probed [61], although the increased ohmic drop in the meniscus configuration (Fig. 6b) may contribute to the lesser shift in the liquid phase water peak at higher applied potentials. In contrast, the BE of the La and Co core levels remain constant (Fig. S14b), indicating the surface of the Sr20 electrocatalyst behaves as a metal under these conditions, a desirable quality for oxygen electrocatalysis. These findings are consistent with the moderate conductivity from Hall measurements for the same composition, and suggests charge transport alone is not limiting kinetics.

### 3.4.3 Changes in Surface Speciation with Applied Potential

The surface adsorbates of carbonates and hydroxyl species observed in a humid environment persist when the electrode is immersed in the KOH electrolyte and polarized to both ORR and OER conditions. Further confirmation of the presence of carbonates can be observed from the C 1s spectra

(Fig. 9a), where the approximately constant BE of the oxidized carbon species at  $\sim 288.5$  eV confirms this is located at least in part on the electrode surface (which is grounded to the analyzer). This is in contrast to adventitious carbon (AC), the BE of which changes with applied potential, suggesting it is located within (or on top of) the water layer. The  $\text{CO}_3$  intensity in both the C 1s and O 1s spectra increase at oxidizing potentials, in contrast to the  $\text{H}_2\text{O}_{\text{liq}}$  intensity in the O 1s from the electrolyte meniscus (Fig. 9b), corroborating its presence on the electrode surface. A first approximation of the extent of  $\text{CO}_3$  coverage can be obtained from the ratio relative to OH species on the catalyst surface. Accounting for the difference in oxygen stoichiometry, the intensity in the O 1s of  $\text{CO}_3$  is half that of OH at 0.8 V applied, consistent with previous findings that the  $\text{CO}_3$  coverage in humid conditions on Sr0 is  $\sim 0.3$  monolayers (ML) while that of OH is  $\sim 0.6$  ML [35]. The presence of  $\text{CO}_3$  species in operando during conditions of oxygen electrocatalysis highlights that a catalyst's affinity for carbonaceous species may be an important parameter in determining the number of available sites for the adsorption of  $\text{O}_2$  or  $\text{OH}^-$  reactants and the binding strength at these sites through possible adsorbate–adsorbate interactions. The qualitative increase of OH under OER conditions further validates the in situ findings that the presence of this adsorbate is linked with OER activity, both of which were maximum for Sr40. For oxides with

facile charge transfer, the reaction mechanism could be limited by proton transfer, consistent with the observation that OER is pH-dependent for highly covalent cobalt oxides [30].

### 3.4.4 Electrocatalyst Stoichiometry

The presence of a bulk electrolyte at high pH and electrode polarization could have dramatic impacts on the surface composition of the film in operando, previously inaccessible by in situ measurements. We first consider the A-site stoichiometry (Fig. 10), as gaseous oxidizing environments have been reported to promote Sr segregation to the surface [58]. The integrated area of the Sr 3d normalized by the sum of the Sr 3d and La 4d remained approximately constant as a function of applied potential (Fig. S15), suggesting the surface composition remains unchanged during ORR and OER. This is consistent with post mortem analysis of Sr40 particles after extensive cycling for the OER, which indicate a stable surface [62]. The B-to-A site ratio (measured by the Co area normalized to the sum of Co, La, and Sr areas), also remains similar with applied potential, although some attenuation is observed at 0.2, 0.6, and 0.7 V likely resulting from increased carbon (Fig. 10), where the decrease in AC at higher potentials could arise from carbon oxidation at the electrode. The perovskite unit cell is composed of alternating layers of AO and  $\text{BO}_2$  planes, and can terminate with

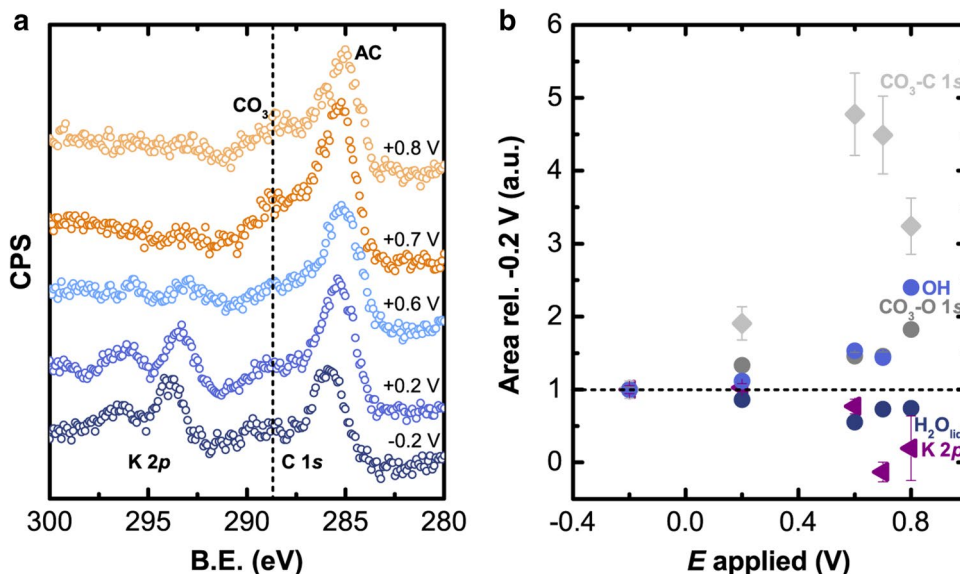


**Fig. 9** **a** C 1s and K 2p spectra in operando for Sr20, normalized to the intensity of the background at 305 eV and offset for clarity. Both adventitious carbon (AC) and the K 2p shift to lower BE with increasing applied potential, and at highly oxidizing conditions, electrostatics and a thinning meniscus layer reduce the K 2p intensity. Oxidized carbon, such as  $\text{CO}_3$ , does not shift with applied potential—indicating it is present on the electrode as opposed to in the electrolyte—and is present under all conditions. **b** Integrated area for Sr20 of the  $\text{CO}_3$  component in the C 1s and O 1s, the K 2p, and the  $\text{H}_2\text{O}_{\text{liq}}$

component in the O 1s relative to that at  $-0.2$  V.  $\text{CO}_3$  shows a relative increase at oxidizing potentials, in contrast to the liquid water layer that decreases due to evaporation, confirming  $\text{CO}_3$  is located on the electrode surface rather than in the electrolyte. Error bars were obtained from the propagated errors of the standard deviation from a single collection scan in CasaXPS, and the areas are obtained from an average of multiple scans. The applied voltage shown vs. the Pt counter electrode corresponds to  $\sim 1$  V versus RHE at 0 V versus Pt

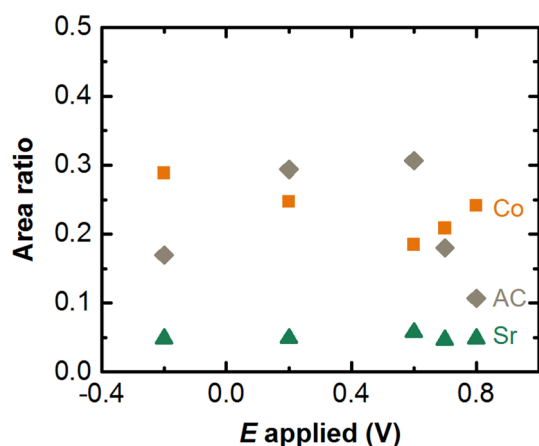


**Fig. 10** Normalized area ratio of Sr20 for the A-site quantified by Sr 3*d*/(La 4*d*+Sr 3*d*) (green up triangle), the B-site quantified by Co 2*p*/(La 4*d*+Sr 3*d*+Co 2*p*) (orange square), and adventitious carbon (AC) in the C 1*s*/(La 4*d*+Sr 3*d*+Co 2*p*) (gray diamonds). The stoichiometry of Sr20 remains similar throughout the polarization, where changes in the Co ratio may be impacted by attenuation from increased AC at 0.2, 0.6, and 0.7 V applied due to the smaller kinetic energy of Co 2*p* versus Sr 3*d* photoelectrons

either layer or a mixed termination. While we cannot assess the termination with the present operando measurements due to uncertainties in the elemental cross sections and meniscus layer thickness, the relatively constant *B*-to-*A* site ratio further reinforces the idea that the surface is stable under OER conditions, and suggests the termination may remain constant across the potential range considered.

Changes in the integrated peak intensities relative to the most reducing conditions can establish overall differences in the composition of the analyzed area, including

the electrolyte. At oxidizing potentials, the K 2*p* intensity decreases (Fig. S15a). While it is challenging to disentangle potential contributions from decreasing meniscus layer thickness (Fig. S13), such a decrease in K 2*p* at oxidizing voltages is consistent with positively charged ions being driven from the double layer [63]. In contrast, the integrated area of the electrode cations La, Sr, and Co increase somewhat at oxidizing potentials (Fig. S15b), possibly due to changes in the meniscus thickness with evaporation, although the ratio between cations is approximately constant (Fig. 10).

## 4 Conclusions

Through the study of (001)-oriented epitaxial LSCO films, we have linked intrinsic catalytic activity to charge transport properties (Fig. 11a), and probed the relationship between electronic structure and surface speciation. High OER activity, maximum for Sr40, is observed for LSCO films with both high carrier density (related to band filling) and carrier mobility (related to metal–oxygen covalency), consistent with previous work [64] illustrating the importance of both O 2*p*-band filling and metal–oxygen covalency descriptors in designing active catalysts. Insight into the reaction mechanism can be obtained through studies on how Sr incorporation impacts the oxygenated species present on the surface in a humid environment, probed using soft X-rays with an information depth on the order of nanometers. Considering a range of oxide chemistries in the LSCO family, as well as different chemical potentials of water, strengthens the assignment of the observed surface species: OH from dissociative adsorption of water, undercoordinated oxygen

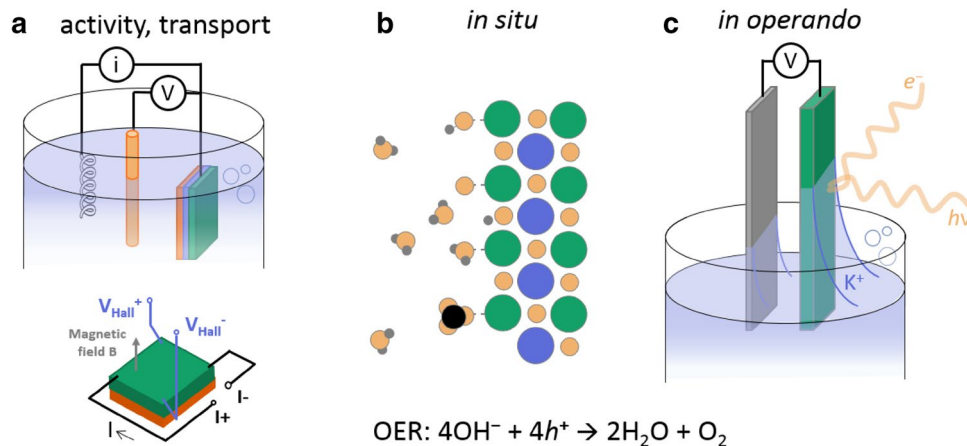


**Fig. 11** Schematics of the parallel approaches that together shed light on LSCO OER activity. **a** Intrinsic OER activity measurement and use of Hall measurements to extract transport properties. **b** Surface species observed on the LSCO surface in situ, in a humid environ-

ment: hydroxyl species, undercoordinated oxygen, adsorbed water, carbonates, and gas phase water. **c** Operando measurements of Sr20, where the surface speciation and composition is elucidated during OER in 0.1 M KOH electrolyte

species, adsorbed water, and  $\text{CO}_3$  from interaction with trace  $\text{CO}_2$  (Fig. 11b). The affinity for hydroxyl species, a key intermediate in OER, increases with Sr content to reach a maximum at Sr40. This trend with Sr content suggests OH formation may be driven by the filling of oxygen vacancies and/or the reduction of  $\text{Co}^{4+}$  to  $\text{Co}^{3+}$  under high RH, consistent with the correlation of OH coverage with hole mobility.

Aided by this understanding of surface chemistry in situ, we then consider operando measurements for the 20% Sr substituted LSCO surface. The use of a liquid electrolyte in a meniscus layer configuration (Fig. 11c) necessitates a “tender” X-ray source, increasing the information depth to tens of nanometers. While this reduces the signal from the electrode surface and leads to a large O 1s peak from liquid water, the surface species can still be investigated with the aid of in situ fitting parameters. In alkaline electrolyte (pH = 13), hydroxyl species remain present at the surface under potentials ranging from ORR to OER conditions. These findings emphasize the importance of OH in the OER reaction mechanism, where the most active Sr40 film also had the highest propensity for hydroxylation in a humid environment. Furthermore, carbonate species are located on the electrolyte surface, potentially impacting the availability of sites for oxygen electrocatalysis or the wettability of the surface. The cation ratio remains unchanged with polarization, indicating a stable surface in operando. In contrast to in situ measurements, where the oxide core levels shifted to higher BE with RH from potential downward band bending, in a liquid electrolyte the Sr20 surface behaves as a metal, with the voltage drop occurring fully in the electrolyte (as opposed to band bending within the electrode). The metallic-like behavior of the catalyst, coupled with the high conductivity from Hall measurements, suggests charge transport alone is not limiting kinetics. Coupled with the accumulation of hydroxyl species at oxidative potentials, operando studies suggest that for covalent oxides with facile charge transfer, the reaction mechanism could be limited by proton transfer. These findings motivate future mechanistic studies of surface charge transfer to adsorbed intermediates to fully understand the nature of the rate limiting step.

These insights into the surface chemistry of perovskite oxide surfaces during oxygen electrocatalysis in alkaline electrolyte bring new understanding into the reactive surface, which is a complex mixture of oxygen-containing adsorbates, and the distribution of the applied potential across the solid/liquid interface. Furthermore, the observed stability of the LSCO under OER conditions experimentally takes into account potential stabilization of the surface from adsorbates and the kinetic hindrances to forming new surfaces, providing insight far beyond that of a traditional Pourbaix diagram. The coupling of in situ and in operando AP-XPS to measurements of the intrinsic activity and transport measurements on epitaxial thin films brings chemical understanding to the

oxide surface and electrochemical interface that will guide future modeling of realistic electrocatalyst surfaces and the OER mechanism.

**Acknowledgements** This work was partially supported by the Skoltech-MIT Center for Electrochemical Energy and the Cooperative Agreement between the Masdar Institute, Abu Dhabi, UAE and MIT (02/MI/MIT/CP/11/07633/GEN/G/00). K.A.S. was supported in part by the Linus Pauling Distinguished Post-doctoral Fellowship at Pacific Northwest National Laboratory (PNNL LDRD 69319). PNNL is a multiprogram national laboratory operated for DOE by Battelle. This research used beamlines 9.3.2 and 9.3.1 at the Advanced Light Source, which is a DOE Office of Science User Facility under contract no. DE-AC02-05CH11231. The PLD film growth was conducted at the Center for Nanophase Materials Sciences, a DOE Office of Science User Facility.

## References

1. Suntivich J, Gasteiger HA, Yabuuchi N, Nakanishi H, Goodenough JB, Shao-Horn Y (2011) Design principles for oxygen-reduction activity on perovskite oxide catalysts for fuel cells and metal–air batteries. *Nat Chem* 3(7):546–550
2. Suntivich J, May KJ, Gasteiger HA, Goodenough JB, Shao-Horn Y (2011) A perovskite oxide optimized for oxygen evolution catalysis from molecular orbital principles. *Science* 334(6061):1383–1385
3. Bockris JOM, Otagawa T (1984) The electrocatalysis of oxygen evolution on perovskites. *J Electrochem Soc* 131(2):290–302
4. Meadowcroft DB (1970) Low-cost oxygen electrode material. *Nature* 226(5248):847–848
5. Matsumoto Y, Yoneyama H, Tamura H (1977) Influence of the nature of the conduction band of transition metal oxides on catalytic activity for oxygen reduction. *J Electroanal Chem Interfacial Electrochem* 83(2):237–243
6. Hibbert DB, Tseung ACC (1978) Homomolecular oxygen exchange and the electrochemical reduction of oxygen on semiconducting oxides. *J Electrochem Soc* 125(1):74–78
7. Larsson R, Johansson LY (1990) On the catalytic properties of mixed oxides for the electrochemical reduction of oxygen. *J Power Sources* 32(3):253–260
8. Peña MA, Fierro JLG (2001) Chemical structures and performance of perovskite oxides. *Chem Rev* 101(7):1981–2018
9. Man IC, Su H-Y, Calle-Vallejo F, Hansen HA, Martínez JI, Inoglu NG, Kitchin J, Jaramillo TF, Nørskov JK, Rossmeisl J (2011) Universality in oxygen evolution electrocatalysis on oxide surfaces. *ChemCatChem* 3(7):1159–1165
10. Hong WT, Risch M, Stoerzinger KA, Grimaud A, Suntivich J, Shao-Horn Y (2015) Toward the rational design of non-precious transition metal oxides for oxygen electrocatalysis. *Energy Environ Sci* 8(5):1404–1427
11. Fabbri E, Haberer A, Walter K, Kotz R, Schmidt TJ (2014) Developments and perspectives of oxide-based catalysts for the oxygen evolution reaction. *Catal Sci Technol* 4(11):3800–3821
12. Vojvodic A, Nørskov JK (2011) Optimizing perovskites for the water-splitting reaction. *Science* 334(6061):1355–1356
13. Malkhandi S, Yang B, Manohar AK, Manivannan A, Prakash GKS, Narayanan SR (2012) Electrocatalytic properties of nanocrystalline calcium-doped lanthanum cobalt oxide for bifunctional oxygen electrodes. *J Phys Chem Lett* 3(8):967–972
14. Zhu Y, Zhou W, Chen Z-G, Chen Y, Su C, Tadé MO, Shao Z (2015)  $\text{SrNb}_{0.1}\text{Co}_{0.7}\text{Fe}_{0.2}\text{O}_{3-8}$  perovskite as a next-generation



- electrocatalyst for oxygen evolution in alkaline solution. *Angew Chem Int Ed* 54(13):3897–3901
15. Sunarso J, Torriero AAJ, Zhou W, Howlett PC, Forsyth M (2012) Oxygen reduction reaction activity of La-based perovskite oxides in alkaline medium: a thin-film rotating ring-disk electrode study. *J Phys Chem C* 116(9):5827–5834
  16. Grimaud A, May KJ, Carlton CE, Lee Y-L, Risch M, Hong WT, Zhou J, Shao-Horn Y (2013) Double perovskites as a family of highly active catalysts for oxygen evolution in alkaline solution. *Nat Comm* 4:2439
  17. Stoerzinger KA, Choi WS, Jeon H, Lee HN, Shao-Horn Y (2015) Role of strain and conductivity in oxygen electrocatalysis on LaCoO<sub>3</sub> thin films. *J Phys Chem Lett* 6(3):487–492
  18. Conder K, Pomjakushina E, Soldatov A, Mitberg E (2005) Oxygen content determination in perovskite-type cobaltates. *Mater Res Bull* 40(2):257–263
  19. Bychkov SF, Sokolov AG, Popov MP, Nemudry AP (2016) Relation between oxygen stoichiometry and thermodynamic properties and the electronic structure of nonstoichiometric perovskite La<sub>0.6</sub>Sr<sub>0.4</sub>CoO<sub>3-d</sub>. *Phys Chem Chem Phys* 18(42):29543–29548
  20. Takeda Y, Kanno R, Takada T, Yamamoto O, Takano M, Bando Y (1986) Phase relation and oxygen-non-stoichiometry of perovskite-like compound SrCoO<sub>x</sub> (2.29 < x < 2.80). *Z Anorg Allg Chem* 540(9–10):259–270.
  21. Sunstrom JE, Ramanujachary KV, Greenblatt M, Croft M (1998) The synthesis and properties of the chemically oxidized perovskite, La<sub>1-x</sub>Sr<sub>x</sub>CoO<sub>3-δ</sub> (0.5 ≤ x ≤ 0.9). *J Solid State Chem* 139(2):388–397
  22. Cheng X, Fabbri E, Nachtegaal M, Castelli IE, El Kazzi M, Haumont R, Marzari N, Schmidt TJ (2015) Oxygen evolution reaction on La<sub>1-x</sub>Sr<sub>x</sub>CoO<sub>3</sub> perovskites: a combined experimental and theoretical study of their structural, electronic, and electrochemical properties. *Chem Mater* 27(22):7662–7672
  23. Hidehito O, Tetsuichi K, Tetsuo G (1974) Crystallographic, electric and thermochemical properties of the perovskite-type Ln<sub>1-x</sub>Sr<sub>x</sub>CoO<sub>3</sub> (Ln: lanthanoid element). *Jpn J Appl Phys* 13(1):1
  24. Kudo T, Obayashi H, Gejo T (1975) Electrochemical behavior of the perovskite-type Nd<sub>1-x</sub>Sr<sub>x</sub>CoO<sub>3</sub> in an aqueous alkaline solution. *J Electrochem Soc* 122(2):159–163
  25. Jain AN, Tiwari SK, Singh RN, Chartier P (1995) Low-temperature synthesis of perovskite-type oxides of lanthanum and cobalt and their electrocatalytic properties for oxygen evolution in alkaline solutions. *J Chem Soc Faraday Trans* 91(12):1871–1875
  26. Mefford JT, Rong X, Abakumov AM, Hardin WG, Dai S, Kolpak AM, Johnston KP, Stevenson KJ (2016) Water electrolysis on La<sub>1-x</sub>Sr<sub>x</sub>CoO<sub>3-δ</sub> perovskite electrocatalysts. *Nat Comm* 7:11053
  27. Miyahara Y, Miyazaki K, Fukutsuka T, Abe T (2016) Influence of surface orientation on the catalytic activities of La<sub>0.8</sub>Sr<sub>0.2</sub>CoO<sub>3</sub> crystal electrodes for oxygen reduction and evolution reactions. *ChemElectroChem* 3(2):214–217
  28. Stoerzinger KA, Lü W, Li C, Venkatesan T, Shao-Horn Y (2015) Highly active epitaxial La<sub>(1-x)</sub>Sr<sub>x</sub>MnO<sub>3</sub> surfaces for the oxygen reduction reaction: role of charge transfer. *J Phys Chem Lett* 6(8):1435–1440
  29. Rong X, Parolin J, Kolpak AM (2016) A fundamental relationship between reaction mechanism and stability in metal oxide catalysts for oxygen evolution. *ACS Catal* 6(2):1153–1158
  30. Grimaud A, Diaz-Morales O, Han B, Hong WT, Lee Y-L, Giordano L, Stoerzinger KA, Koper MTM, Shao-Horn Y (2017) Activating lattice oxygen redox reactions in metal oxides to catalyze oxygen evolution. *Nat Chem* 9:457–465
  31. Stoerzinger KA, Hong WT, Crumlin EJ, Bluhm H, Shao-Horn Y (2015) Insights into electrochemical reactions from ambient pressure photoelectron spectroscopy. *Acc Chem Res* 48(11):2976–2983
  32. Crumlin EJ, Liu Z, Bluhm H, Yang W, Guo J, Hussain Z (2015) X-ray spectroscopy of energy materials under in situ/operando conditions. *J Electron Spectrosc Relat Phenom* 200:264–273
  33. Lena T, Ashley RH, Osman K, Line K, Hendrik B (2017) Ambient pressure photoelectron spectroscopy: practical considerations and experimental frontiers. *J Phys Condens Matter* 29(5):053002
  34. Yamamoto S, Bluhm H, Andersson K, Ketteler G, Ogasawara H, Salmeron M, Nilsson A (2008) In situ X-ray photoelectron spectroscopy studies of water on metals and oxides at ambient conditions. *J Phys Condens Matter* 20(18):184025
  35. Stoerzinger KA, Hong WT, Crumlin EJ, Bluhm H, Biegalski MD, Shao-Horn Y (2014) Water reactivity on the LaCoO<sub>3</sub> (001) surface: an ambient pressure X-ray photoelectron spectroscopy study. *J Phys Chem C* 118(34):19733–19741
  36. Stoerzinger KA, Hong WT, Azimi G, Giordano L, Lee Y-L, Crumlin EJ, Biegalski MD, Bluhm H, Varanasi KK, Shao-Horn Y (2015) Reactivity of perovskites with water: role of hydroxylation in wetting and implications for oxygen electrocatalysis. *J Phys Chem C* 119:18504–18512
  37. Axnanda S, Crumlin EJ, Mao B, Rani S, Chang R, Stolte W, Karlsson PG, Edwards MOM, Lundqvist M, Moberg R, Ross PN, Hussain Z, Liu Z (2015) Using “tender” X-ray ambient pressure X-ray photoelectron spectroscopy as a direct probe of solid-liquid interface. *Sci Rep* 5:9788
  38. Karsloglu O, Nemsak S, Zegkinoglou I, Shavorskiy A, Hartl M, Salmassi F, Gullikson EM, Ng ML, Rameshan C, Rude B, Bianculli D, Cordones AA, Axnanda S, Crumlin EJ, Ross PN, Schneider CM, Hussain Z, Liu Z, Fadley CS, Bluhm H (2015) Aqueous solution/metal interfaces investigated in operando by photoelectron spectroscopy. *Faraday Discuss* 180:35–53
  39. Ali-Löyty H, Louie MW, Singh MR, Li L, Sanchez Casalongue HG, Ogasawara H, Crumlin EJ, Liu Z, Bell AT, Nilsson A, Friebel D (2016) Ambient-pressure XPS study of a Ni-Fe electrocatalyst for the oxygen evolution reaction. *J Phys Chem C* 120(4):2247–2253
  40. Lichterman MF, Hu S, Richter MH, Crumlin EJ, Axnanda S, Favaro M, Drisdell W, Hussain Z, Mayer T, Brunschwig BS, Lewis NS, Liu Z, Lewerenz H-J (2015) Direct observation of the energetics at a semiconductor/liquid junction by operando X-ray photoelectron spectroscopy. *Energy Environ Sci* 8(8):2409–2416
  41. Favaro M, Jeong B, Ross PN, Yano J, Hussain Z, Liu Z, Crumlin EJ (2016) Unravelling the electrochemical double layer by direct probing of the solid/liquid interface. *Nat Comm* 7:12695
  42. van der Pauw LJ (1958) A method of measuring the resistivity and Hall coefficient on lamellae of arbitrary shape. *Philips Tech Rev* 8:220–224
  43. Grass ME, Karlsson PG, Aksoy F, Lundqvist M, Wannberg B, Mun BS, Hussain Z, Liu Z (2010) New ambient pressure photoemission endstation at Advanced Light Source beamline 9.3.2. *Rev Sci Instrum* 81(5):053106
  44. Kawazoe H, Yasukawa M, Hyodo H, Kurita M, Yanagi H, Hosono H (1997) P-type electrical conduction in transparent thin films of CuAlO<sub>2</sub>. *Nature* 389(6654):939–942
  45. Suntivich J, Hong WT, Lee Y-L, Rondinelli JM, Yang W, Goodenough JB, Dabrowski B, Freeland JW, Shao-Horn Y (2014) Estimating hybridization of transition metal and oxygen states in perovskites from O K-edge X-ray absorption spectroscopy. *J Phys Chem C* 118(4):1856–1863
  46. Hautier G, Miglio A, Ceder G, Rignanese G-M, Gonze X (2013) Identification and design principles of low hole effective mass p-type transparent conducting oxides. *Nat Comm* 4:2292
  47. Risch M, Stoerzinger KA, Maruyama S, Hong WT, Takeuchi I, Shao-Horn Y (2014) La<sub>0.8</sub>Sr<sub>0.2</sub>MnO<sub>3-δ</sub> decorated with Ba<sub>0.5</sub>Sr<sub>0.5</sub>Co<sub>0.8</sub>Fe<sub>0.2</sub>O<sub>3-δ</sub>: a bifunctional surface for oxygen electrocatalysis with enhanced stability and activity. *J Am Chem Soc* 136(14):5229–5232

48. Imamura M, Matsubayashi N, Shimada H (2000) Catalytically active oxygen species in  $\text{La}_{1-x}\text{Sr}_x\text{CoO}_{3-\delta}$  studied by XPS and XAFS spectroscopy. *J Phys Chem B* 104(31):7348–7353
49. van der Heide PAW (2002) Systematic X-ray photoelectron spectroscopic study of  $\text{La}_{1-x}\text{Sr}_x$ -based perovskite-type oxides. *Surf Interface Anal* 33(5):414–425
50. Hong WT, Stoerzinger KA, Crumlin EJ, Mutoro E, Jeon H, Lee HN, Shao-Horn Y (2016) Near-ambient pressure XPS of high-temperature surface chemistry in  $\text{Sr}_2\text{Co}_2\text{O}_5$  thin films. *Top Catal* 59(5):574–582
51. Petitto SC, Marsh EM, Carson GA, Langel MA (2008) Cobalt oxide surface chemistry: the interaction of  $\text{CoO}(1\ 0\ 0)$ ,  $\text{Co}_3\text{O}_4(1\ 1\ 0)$  and  $\text{Co}_3\text{O}_4(1\ 1\ 1)$  with oxygen and water. *J Mol Catal A* 281(1–2):49–58
52. Stoerzinger KA, Comes R, Spurgeon SR, Thevuthasan S, Ihm K, Crumlin EJ, Chambers SA (2017) Influence of  $\text{LaFeO}_3$  surface termination on water reactivity. *J Phys Chem Lett* 8(5):1038–1043
53. Tascon JMD, Tejuca LG (1981) Adsorption of  $\text{CO}_2$  on the perovskite-type oxide  $\text{LaCoO}_3$ . *J Chem Soc Faraday Trans 1* 77(3):591–602
54. Axnanda S, Scheele M, Crumlin E, Mao B, Chang R, Rani S, Faiz M, Wang S, Alivisatos AP, Liu Z (2013) Direct work function measurement by gas phase photoelectron spectroscopy and its application on PbS nanoparticles. *Nano Lett* 13(12):6176–6182
55. Tsvetkov N, Lu Q, Sun L, Crumlin EJ, Yildiz B (2016) Improved chemical and electrochemical stability of perovskite oxides with less reducible cations at the surface. *Nat Mater* 15(9):1010–1016
56. Hong WT, Stoerzinger KA, Moritz B, Devereaux TP, Yang W, Shao-Horn Y (2015) Probing  $\text{LaMO}_3$  metal and oxygen partial density of states using X-ray emission, absorption, and photoelectron spectroscopy. *J Phys Chem C* 119(4):2063–2072
57. Krischok S, Höfft O, Günster J, Stultz J, Goodman DW, Kempter V (2001)  $\text{H}_2\text{O}$  interaction with bare and Li-precovered  $\text{TiO}_2$ : studies with electron spectroscopies (MIES and UPS (HeI and II)). *Surf Sci* 495(1–2):8–18
58. Crumlin EJ, Mutoro E, Liu Z, Grass ME, Biegalski MD, Lee Y-L, Morgan D, Christen HM, Bluhm H, Shao-Horn Y (2012) Surface strontium enrichment on highly active perovskites for oxygen electrocatalysis in solid oxide fuel cells. *Energy Environ Sci* 5(3):6081–6088
59. Sunding MF, Hadidi K, Diplas S, Løvvik OM, Norby TE, Gunnæs AE (2011) XPS characterisation of in situ treated lanthanum oxide and hydroxide using tailored charge referencing and peak fitting procedures. *J Electron Spectrosc Relat Phenom* 184(7):399–409
60. Feng ZA, Balaji Gopal C, Ye X, Guan Z, Jeong B, Crumlin E, Chueh WC (2016) Origin of overpotential-dependent surface dipole at  $\text{CeO}_{2-x}$ /gas interface during electrochemical oxygen insertion reactions. *Chem Mater* 28(17):6233–6242
61. Stoerzinger KA, Favaro M, Ross PN, Yano J, Liu Z, Hussain Z, Crumlin EJ (2018) Probing the surface of platinum during the hydrogen evolution reaction in alkaline electrolyte. *J Phys Chem B* 122(2):864–870
62. May KJ, Carlton CE, Stoerzinger KA, Risch M, Suntivich J, Lee Y-L, Grimaud A, Shao-Horn Y (2012) Influence of oxygen evolution during water oxidation on the surface of perovskite oxide catalysts. *J Phys Chem Lett* 3(22):3264–3270
63. Grahame DC, Soderberg BA (1954) Ionic Components of charge in the electrical double layer. *J Chem Phys* 22(3):449–460
64. Hong WT, Welsch RE, Shao-Horn Y (2016) Descriptors of oxygen-evolution activity for oxides: a statistical evaluation. *J Phys Chem C* 120(1):78–86